

Illuminating strongly interacting matter

Daniel Watts

*University of Edinburgh, Institute for Particle and Nuclear Physics, James Clerk
Maxwell Building, King's buildings, Mayfield Road, Edinburgh, UK*

ABSTRACT

Intermediate energy (\sim GeV) photons are an ideal probe for studying the properties of strongly interacting matter from the nuclear scale down to the sub-nuclear components of the nucleus. This lecture gives an introduction to a few selected topics in this broad field. Including programmes to improve our knowledge of the matter distribution of nuclei and the excitation spectrum of the nucleon.

I – Photon beam facilities

The quality and intensity of photon beams has increased dramatically in recent decades. Continuous (100%) duty factor beams have been developed with good energy resolution (up to 0.1 MeV) and a high degree of polarisation. These advances have made possible many experiments using electromagnetic probes which could not previously be attempted. The physics interpretation of such experiments benefit greatly from the use of electromagnetic probes: (i) minimal initial state interactions of the probe with the target of interest (ii) well understood interaction (quantum electrodynamics) and (iii) a weak interaction strength in the nuclear medium ensuring surface absorption and associated shadowing effects can be neglected.

The generation of the intense photon beam starts with the production of a high quality electron beam. Facilities currently in operation use 2 techniques. In the microtron technique the electron beam is recirculated through linear accelerating sections (linacs) many times, with the orbits through the recirculating magnets tuned such that the electrons arrive in phase with the rf field in the linacs. The leading microtron facilities are the MAMI microtron in Mainz, Germany [1] and the CEBAF microtron at Jefferson Lab [2] in Virginia, USA. A schematic and photograph of one of the four microtron stages making up the MAMI accelerator is shown in Fig. 1. Schematics of the MAMI and JLAB accelerator complexes are shown in Fig. 2.

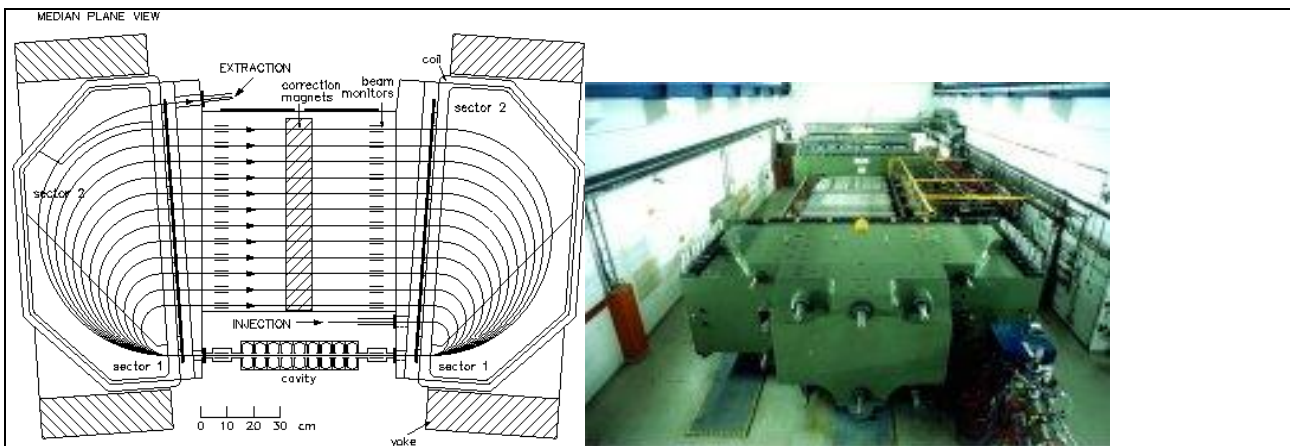


Fig.1: Schematic of a microtron stage from the MAMI accelerator (left) and a picture of the microtron (right). The recirculating magnets are the green metal sections. The recirculating beam pipes can be seen inbetween the magnet sections.

Other techniques include the use of an electron storage ring facility. These can either be specifically built for the purpose (e.g. ELSA at Bonn) or can be piggy-backed onto existing storage rings used as synchrotron sources, such as at the MaxLab at Lund or the SPRING8 facility in Japan. Electron beams extracted from storage rings tend to have somewhat poorer duty factors and emittances than those of microtrons.

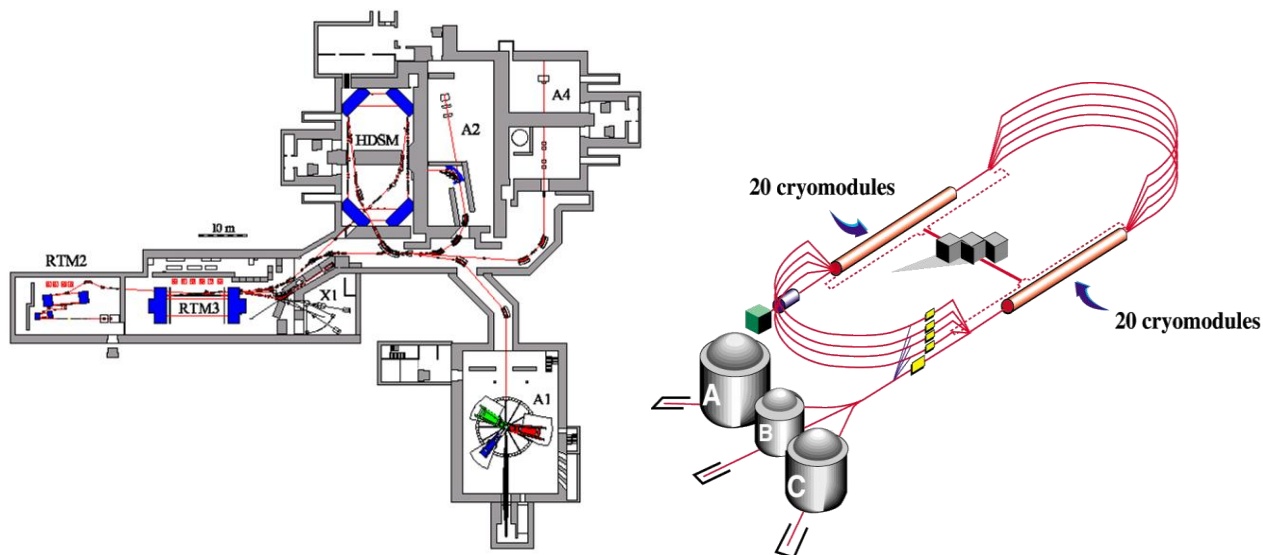


Fig 2: Left: Schematic of the MAMI facility showing the 4 interconnecting microtron stages. The experimental halls are labelled A1 to A4. The real photon experiments are carried out in “Hall A2” Right: The Jefferson Lab facility in Virginia, USA showing the 4 recirculating arcs and the superconducting linac sections.

The photon beam is created from the electron beam using two main techniques, laser backscattering or the bremsstrahlung technique. In Laser Backscattering a low energy (UV/visible) laser beam is fired at the incoming high energy electron beam. A fraction of the photons will undergo large angle backward Compton scattering, producing a usable high energy backscattered photon beam. The bremsstrahlung technique comprises impinging the incident electron beam on a thin metal foil (“radiator”) in which the incident

electrons undergo rapid accelerations in the electric field of the nuclei of the metal atoms in the foil producing bremsstrahlung photons. The energy of the photons are tagged by detecting the scattered bremsstrahlung electron in a magnetic spectrometer. As the incident electron beam energy is well known then the photon energy can be reconstructed from the difference between the incident and scattered electron energies. The magnetic tagging spectrometer used to tag the recoil bremsstrahlung electrons at the MAMI facility is shown in Fig. 3.

The availability of polarisation in the new generation of intense photon beams has opened up many new physics possibilities. Bremsstrahlung facilities can produce photons with high degrees of linear or circular polarisation. The two types of polarisation are indicated in Fig. 3. If an amorphous radiator is used then the bremsstrahlung photons will be unpolarised. Using longitudinally polarised electrons will result in a circularly polarised photon beam. The longitudinally polarised electrons are generally produced at the low energy injection stage of the accelerator by polarised photoelectric effect from a strained GaAs cathode. The use of a crystalline radiator such as diamond, rather than an amorphous metallic radiator, allows for coherent bremsstrahlung processes. These occur when the momentum transfer in the bremsstrahlung process matches the direction of the reciprocal lattice vectors in the crystal. This coherent mechanism produces linear polarisation in the produced photons.

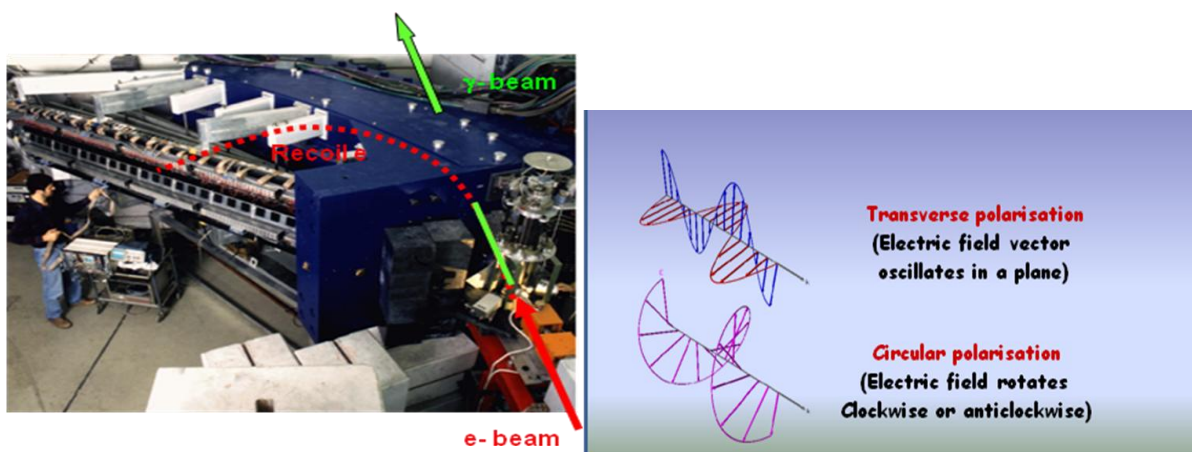








Fig 3: The tagged photon facility at the MAMI electron beam facility. The dipole magnet is shown in blue. The path of the post bremsstrahlung electron through the dipole into the array of focal plane detectors is shown by the dotted line.

A comparison of the major photon beam facilities is given in the table below. These are a guide only and for specific experiments the beam parameters may be optimised. The LEGS and GRAAL facilities have both recently ceased operations.

	E_{γ}^{\max} (GeV)	I_{γ}^{\max} ($s^{-1}MeV^{-1}$)	ΔE_{γ} (FWHM) (MeV)	$Pol_{\gamma}^{\text{lin}}$ (%)	$Pol_{\gamma}^{\text{circ}}$ (%)
	3.5	$\approx 10^4$	5	70	80
	1.5	$\approx 10^3$	15	100	100
Jefferson Lab 	5.4 12	$\approx 10^4$	5	70	80
	0.45	$\approx 10^3$	5	100	100
	0.8 1.6	$\approx 10^5$	1	70	80
	3.0	$\approx 10^3$	30	100	100

2 – Selected physics topics

Two physics topics which utilise the MAMI and JLAB photon beam facilities will now be described. These span different distance scales from the nuclear to the sub nucleon regime. There is a wide user community exploiting the photon beam facilities for topics in nuclear and hadron physics. The topics selected below are biased towards those in which Edinburgh plays a leading role but illustrates the utility of electromagnetic probe experiments.

2.1 The Nuclear matter distribution

Our knowledge of the shape of the nuclei is still incomplete despite many decades of study. The nuclear charge distributions have been measured to a high accuracy in elastic electron scattering experiments, most notably in the 80's. However the distribution of neutrons in the nucleus is known to much poorer accuracy. For example in a typical heavy nucleus like ^{208}Pb the neutron radius is only established to $\sim 0.01\text{-}0.02$ fm despite many measurements using hadronic probes, with the most accurate seemingly coming from recent antiproton measurements [3]. Recent works indicate elastic proton nucleus scattering may not be sensitive to the nature of the neutron skins because of the uncertainties in interpreting the data [4].

This poor knowledge of the neutron distribution in nuclei represents a significant gap in our understanding of nuclear structure. Different theoretical models predict a wide range of values for the difference between the rms radii of neutrons and protons (commonly referred to as the size of the neutron skin). The wide range of values predicted highlights how these theories have not been sufficiently challenged by accurate experimental data. The predictions from various Skyrme and relativistic mean field nuclear calculations are shown in Fig 5, taken from Ref [5,6]. The neutron skin is predicted to range from approximately 0 fm for light nuclei up to 0.3-0.4 fm for heavy nuclei. For ^{208}Pb the various nuclear structure calculations predict skins in the range of ~ 0.05 to ~ 0.35 fm.

Clearly accurate measurements of the neutron skin are needed as a discriminator between the various nuclear theories. However the impact of a measurement is even

more significant when the close correlation between the size of the neutron skin and poorly established parameters in the equation of state for nuclear matter are considered.

For example, the close correlation between the size of the neutron skin and crucial parameters in the nuclear equation of state can clearly be seen from the analyses presented in Fig 5 and 6. The symmetry energy at saturation density (a_4) is poorly established (Atomic data and nuclear data tables put it at 26-34 MeV [7]). Further, a close correlation between the size of the neutron skin and the P_0 parameter (the first derivative of the symmetry energy with respect to density evaluated at nuclear saturation density) is evident. Determining these parameters with accuracy would allow information on the density dependence of the symmetry energy to be better established, giving better extrapolations into regions away from nuclear saturation density such as encountered in neutron stars.

The physics of neutron stars has a common and sensitive dependence on the a_4 and P_0 parameters of the equation of state. Therefore a correlation between the size of the neutron skin in ^{208}Pb and neutron star properties arises. There has been a large quantity of theoretical research in recent years highlighting the impact of neutron skin measurements on neutron stars e.g. [8]). One of these correspondences is presented in Fig. 6 where the size of the neutron skin in ^{208}Pb correlates with the density at which neutron rich matter goes from a liquid to a solid phase.

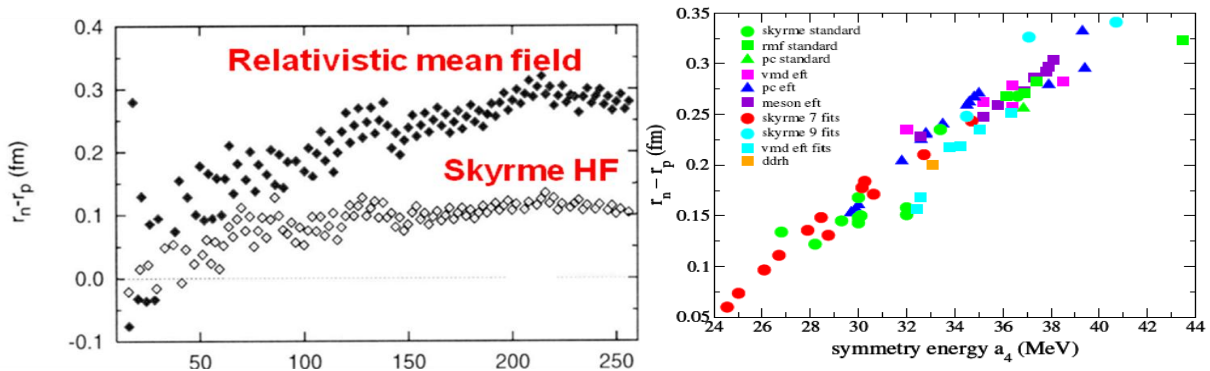


Fig 5: Left: Variation of the predicted neutron skin with nuclear mass number (A). Right: Model predictions based on different theoretical assumptions plotted versus the asymmetry parameter a_4 (MeV) (taken Ref [6])

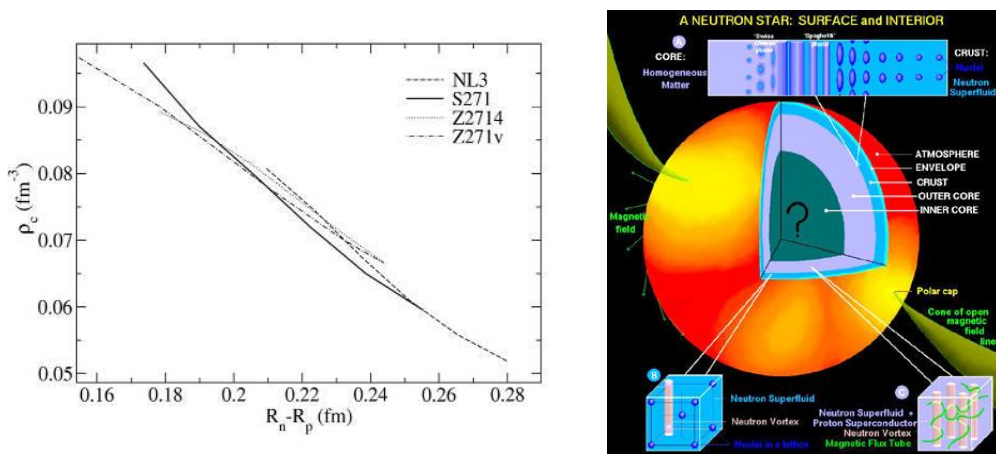


Fig 6: Correlation between neutron skin thickness and neutron star properties. Left: the correlation between neutron skin thickness and the critical density where neutron rich matter goes from solid to liquid phase. Right: Schematic illustration of the structure of a neutron star.

Coherent pion photoproduction from nuclei is an attractive technique to obtain information on the existence and nature of neutron skins in nuclei. The incident probe is close to ideal with little shadowing or initial state interactions (of course a photon probe does not even suffer from the initial state coulomb distortions that are significant in electron scattering from large nuclei). The production of a neutral pion occurs with close to equal probability for both proton and neutron making this reaction a good probe of the matter distribution of the nucleus. In the coherent reaction the amplitudes from pion production from all the nucleons in the nucleus add coherently and a diffraction pattern in the angle of the outgoing pions is observed. In plane wave impulse approximation the cross section directly contains the fourier transform of the matter distribution $|F_m(\mathbf{q})|^2$.

$$d\sigma/d\Omega(\text{PWIA}) = (s/m_N^2) A^2 (q_{\pi^*}/2k_{\gamma}) F_2(E_{\gamma^*}, \theta_{\pi^*})^2 |F_m(\mathbf{q})|^2 \sin^2\theta_{\pi^*}$$

The A^2 scaling of the coherent cross section means that for heavy nuclei such as ^{208}Pb large cross sections result (typically mb).

The measured cross sections will be affected by the pion-nucleus interaction and it is important to try to minimise the effect of this in the analysis as much as possible. The magnitude of these final state interaction effects can be assessed by comparing the PWIA predictions to the full calculations (including pion-nucleus interactions), as presented in Fig. 7. The model calculations are based upon a unitary isobar model of pion photoproduction with final state interactions calculated using a momentum space optical potential, the parameters of which have been tuned to pion-nucleus scattering data [9].

The theoretical predictions illustrate the “window of opportunity” below $E_{\gamma} \sim 190$ MeV where only modest effects from the π -A interaction are expected reflecting the dominant p-wave nature of π -N interaction. Also shown in the figure are the preliminary total coherent cross sections extracted from the new Crystal Ball experiment. The agreement between experiment and theory is good over the full measured energy range giving confidence in the treatment of the production and final state interaction processes in the model.

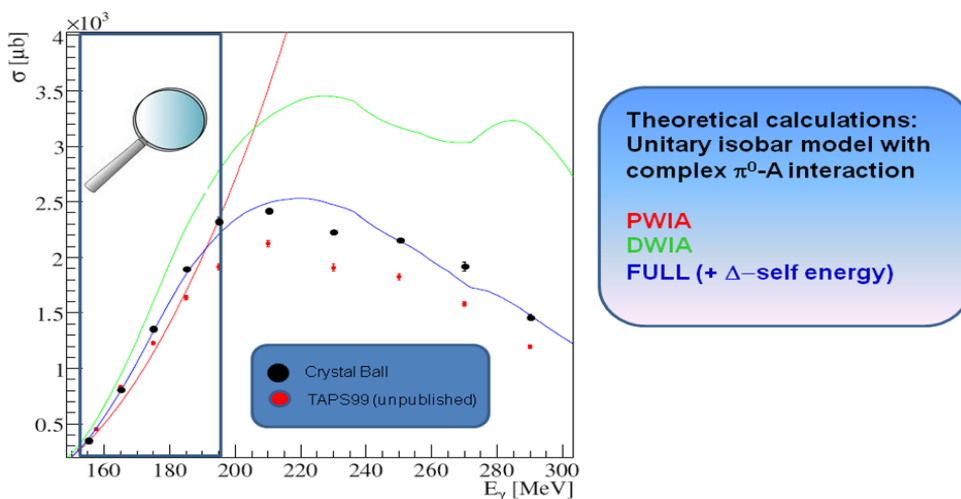


Fig 7: Preliminary results for the $^{208}\text{Pb}(\gamma, \pi^0)^{208}\text{Pb}$ reaction compared to the theoretical predictions of [8]

The extracted cross sections are presented as a function of momentum transfer ($q = P_{\gamma} - P_{\pi^0}$) in Fig 8. The theoretical predictions have been smeared according to the

experimental resolution to allow direct comparison with the experimental data. Good agreement between theory and model is observed.

A first attempt to extract the size of the neutron skin from the measured data involved adjusting the form factor input into the theoretical model. This is in the form of a 2 parameter Fermi function. The charge distribution for ^{208}Pb used the parameters extracted from fits to elastic electron scattering. For the neutron distribution a range of distributions were used with varying rms radii corresponding to skin thicknesses from 0 to 0.5 fm. The neutron skin value which best fits the data is extracted from the best χ^2 fit to the data. Preliminary results shown in Fig 8 indicate reasonably stable predicted skin thicknesses for the data at different incident photon energies. Further work to accurately establish systematics, utilise more detailed form factor shapes, and to extract skins from the data on lighter nuclei are in progress. However, it is apparent the coherent pion technique will be a very promising method to extract this important and fundamental quantity.

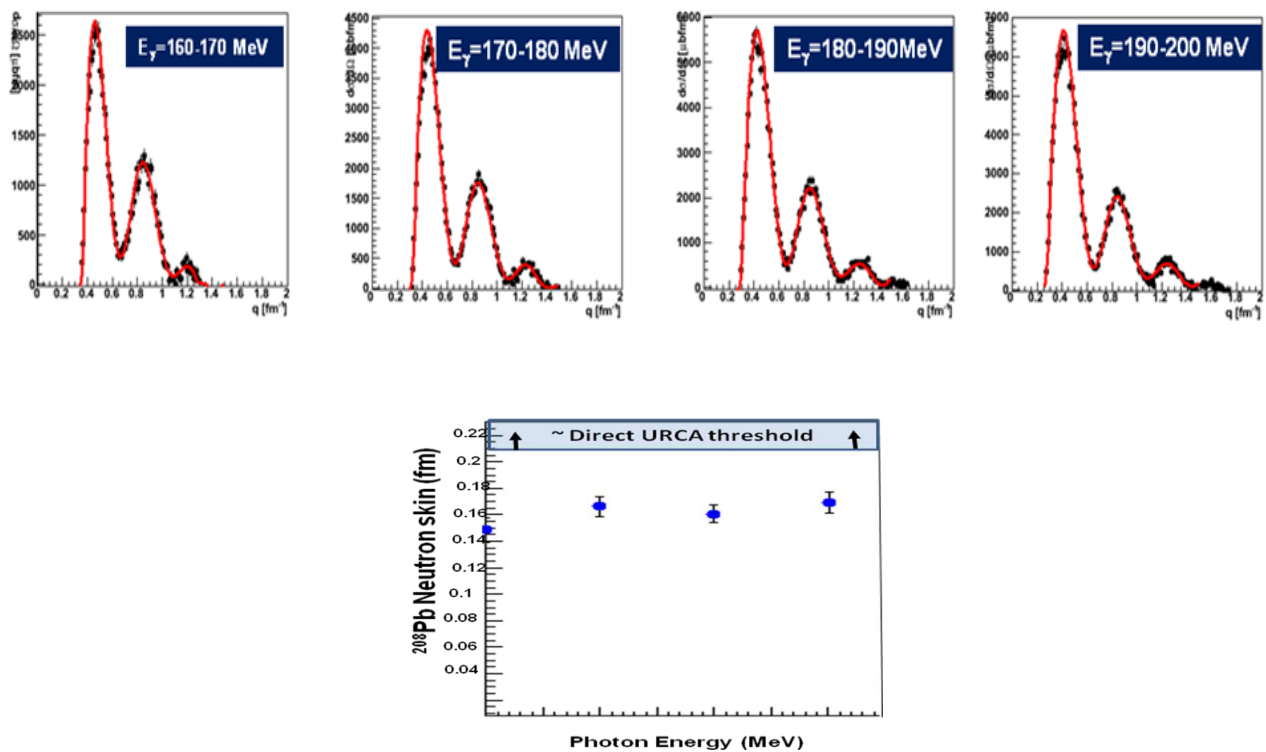


Fig 8: Top: Cross sections as a function of momentum transfer. Bottom: Preliminary extracted skin thicknesses

2.2 The Excitation spectrum of the nucleon

The nucleon is a complicated composite object comprised of three light quarks existing in a sea of virtual gluons and quark-antiquark pairs (Fig 9). The rest mass of the quarks is a few percent of the mass of the nucleon. Most of the mass of the nucleon, and therefore the visible universe, arises from the energy of the interaction of these light quarks with each other and the QCD vacuum.

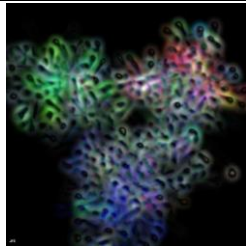


Fig 9: Qualitative picture of the energy density in the nucleon.

The excitation spectrum of the nucleon is a fundamental observable which is sensitive to the dynamics of its constituents. Despite its importance this spectrum is not well established, many resonances have large uncertainties in their mass, width and electromagnetic couplings e.g see ref. [10]. Even the existence of many resonances is uncertain as they give inconsistent signals in different partial wave analyses of the world data set [klempt]. The current experimental situation is shown in Fig 10 for the spectrum of states with isospin 1/2. The shaded boxes show the experimental data with the width of the box showing the uncertainty in the mass of the excited state. Clearly the current status is poor, with even the ordering of many states ambiguous. The colour coding gives indication of the certainty with which the state has been shown to exist, with green shaded resonances classed as “existence uncertain” by the particle data group.

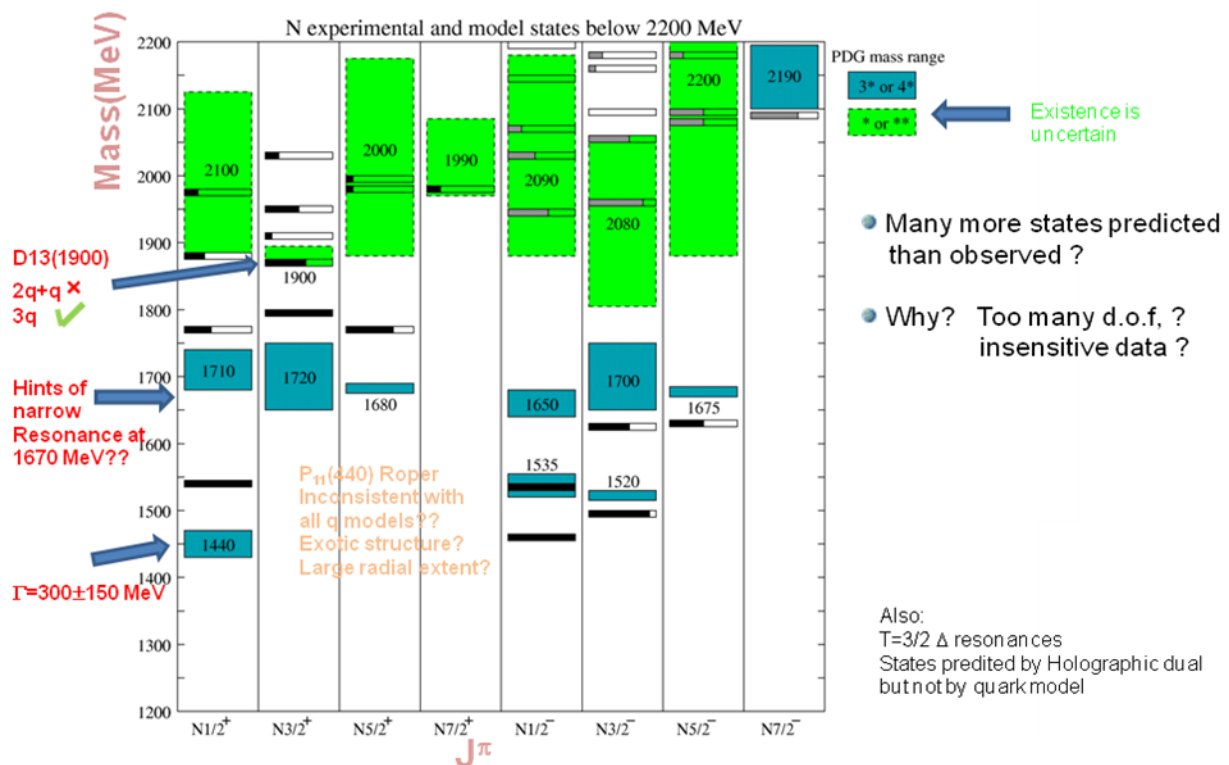


Fig 10: Experimental determination of the resonance spectrum (shaded boxes). The black lines correspond to predictions of the constituent quark model.

This situation is particularly disappointing given the expected progress in the theoretical description of the spectrum currently ongoing and expected in the near future. Most existing predictions are based on constituent quark models [11] in which the degrees of freedom of the nucleon are taken to be quarks with large effective masses (each $\sim 1/3$ the mass of the nucleon). Different assumptions employed in these quark models, such as assuming symmetric or di-quark dynamics, result in different predictions for the

spectrum. However these are not discernible given the present experimental uncertainties. The predictions of the symmetric quark model are also shown in Fig 10. The models tend to do reasonably well describing the low lying part of the excitation spectrum, reproducing the multiplicities of low lying states with different J^π , albeit with poor detailed agreement with the masses. In fact quark models do not reproduce the lowest lying excited state observed in nature. Quark models predict the $\frac{1}{2}^-$ to be the lowest lying state rather than the $\frac{1}{2}^+$ "Roper resonance" observed experimentally.

The phenomenological constituent quark approaches are being complemented in recent years by continuously improving predictions of the excitation spectrum from Lattice QCD [12], being carried out at progressively more realistic light quark masses as computing power increases. Other exciting recent developments include holographic dual theories which employ the higher dimensionality of string theories [13]. Calculations based on QCD using a Dyson-Schwinger approach [14] could be achievable in the near future.

There is a current world effort to improve the quality of experimental information on the excitation spectrum of the nucleon through measurements of meson photoproduction. This is being carried out at facilities including Jefferson Lab, ELSA, MAMI, GRAAL and LEPS. The photon probe is ideal for such studies having the benefit of being polarisable and having a well understood interaction (Quantum Electrodynamics). The main process under study in these reactions is the photoproduction of pseudo-scalar mesons from the nucleon. This process can be described by 4 complex reaction amplitudes which lead to 16 experimental observables. These observables are presented in Fig 11 and comprise the cross section, 3 single polarisation observables corresponding to polarisation of the photon beam (Σ), nucleon target (T) or measurement of recoil nucleon polarisation (P) and three quartets of double-polarisation observables corresponding to simultaneous determination of the polarisation of beam and target, beam and recoil or target and recoil.

Given the long standing uncertainties in resonance properties, largely arising because of the different results between the different partial wave analyses of the existing world data, it is highly desirable to move as close as possible to what is referred to as a "complete measurement" of observables. This represents the measurement of sufficient experimental quantities to fully constrain the 4 basic reaction amplitudes (b_1 to b_4 in fig. 11), enabling a model independent extraction. This full constraint of the magnitude and phases of the amplitudes can be achieved with a minimum of eight measurements, which necessarily involve at least 4 measurements of double-polarisation observables. There have already been major successes in developing circularly and linearly polarised photon beams at the major laboratories. In more recent years there has been great progress in the setup of polarised "frozen spin" nucleon targets, which permit the operation of polarised nucleon targets without large quantities of holding magnet infrastructure limiting the detector acceptance.




























Observable	Polarisation of			
	γ	target	recoil	
1. $\{d\sigma/d\Omega\}/\mathcal{N}$				$= b_1 ^2+ b_2 ^2+ b_3 ^2+ b_4 ^2$
Single polarization				
2. P				$= b_1 ^2- b_2 ^2+ b_3 ^2- b_4 ^2$
3. Σ				$= b_1 ^2+ b_2 ^2- b_3 ^2- b_4 ^2$
4. T				$= b_1 ^2- b_2 ^2- b_3 ^2+ b_4 ^2$
Double polarizatopn				
Beam-target				
5. E				$=2 \operatorname{Re}(b_1 b_3^* + b_2 b_4^*)$
6. F				$=2 \operatorname{Im}(b_1 b_3^* - b_2 b_4^*)$
7. G				$=2 \operatorname{Im}(b_1 b_3^* + b_2 b_4^*)$
8. H				$=-2 \operatorname{Re}(b_1 b_3^* + b_2 b_4^*)$
Beam-recoil				
9. C_x				$=-2 \operatorname{Im}(b_1 b_4^* - b_2 b_3^*)$
10. C_y				$=2 \operatorname{Re}(b_1 b_4^* + b_2 b_3^*)$
11. O_x				$=2 \operatorname{Re}(b_1 b_4^* - b_2 b_3^*)$
12. O_z				$=2 \operatorname{Im}(b_1 b_4^* + b_2 b_3^*)$
Target-recoil				
13. T_x				$=2 \operatorname{Re}(b_1 b_2^* - b_3 b_4^*)$
14. T_z				$=2 \operatorname{Im}(b_1 b_2^* - b_3 b_4^*)$
15. L_x				$=-2 \operatorname{Im}(b_1 b_2^* + b_3 b_4^*)$
16. L_z				$=2 \operatorname{Re}(b_1 b_2^* + b_3 b_4^*)$

Fig 11: The 16 experimental observables in pseudo scalar meson photoproduction. The right hand column show how each observable relates to the 4 fundamental reaction amplitudes.

As an illustration of the power of the new quality measurements to partial wave analysis Fig 12 shows some preliminary data obtained for the Σ beam asymmetry observable for the $n(\gamma, \pi)p$ reaction using the CLAS detector at Jefferson Lab [15]. This is only a small sample of the available data, covering a small angular range. The lines on the plot show the current expectation for the Σ observable from leading partial wave analyses.

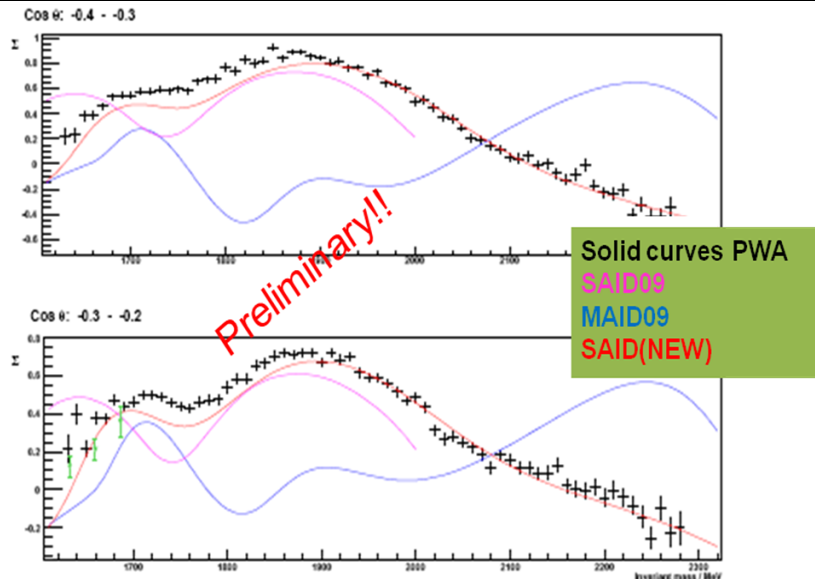


Fig 12: Preliminary data for the Σ observable in the reaction $n(\gamma,\pi)p$ measured using the CLAS detector at Jefferson Lab. Results from partial wave analyses are shown on the figure

It is clear that the current solutions (SAID09 and MAID09) do not describe the new preliminary experimental data well. Inclusion of the new data set in the partial wave analyses will therefore give valuable new constraints. The SAID(NEW) predictions include the new Σ data and, as expected, give better agreement with the measured distributions.

The partial wave analyses are fitted to the world cross section and polarisation datasets and these constraints allows the reaction to be separated into the contributions from different angular momentum, isospin channels. The effect of new preliminary data on the partial wave analysis solutions is indicated in Fig 13.

Analysis of these partial waves to extract resonance properties is an involved task. However the reader can get a feel for what is involved with the simplified prescription described below. The characteristic phase motion as a partial wave passes over an elastic resonance is that there will be a peak in the imaginary part of the partial wave coinciding with a zero in the real part, corresponding to how the propagator for the resonance should be on shell exactly at the resonance position. As seen in Fig. 13 the better established partial waves such as the F_{15} ¹ clearly show established resonances such as the $F_{15}(1680)$. The new data does not affect this partial wave significantly. However the new data appears to significantly alter the partial wave solutions in many other partial waves such as the P_{11} (isospin=1/2, J=1/2), also presented in the figure. As we move nearer to a complete measurement it is hoped that the partial wave analyses will converge, we are hoping to get to the position where a new measurement has little effect on the partial wave solution.

There are major programmes of measurements of beam-target double polarisation observables at MAMI, JLAB and ELSA. However, the complete measurement of observables necessarily also requires measurement of recoil nucleon polarisation. To achieve this a large acceptance recoil polarimeter has been developed by our group for the Crystal Ball at MAMI. This new data will be a valuable and unique contribution to this world programme. In the following sections the data analysis procedures and preliminary results from the recoil nucleon polarimeter from the Crystal Ball at MAMI will be presented.

¹ Spectroscopic notation is $L_{2l} 2J$ therefore F_{15} corresponds to partial wave in which the final nucleon meson state has isospin $1/2$ and $J=5/2$

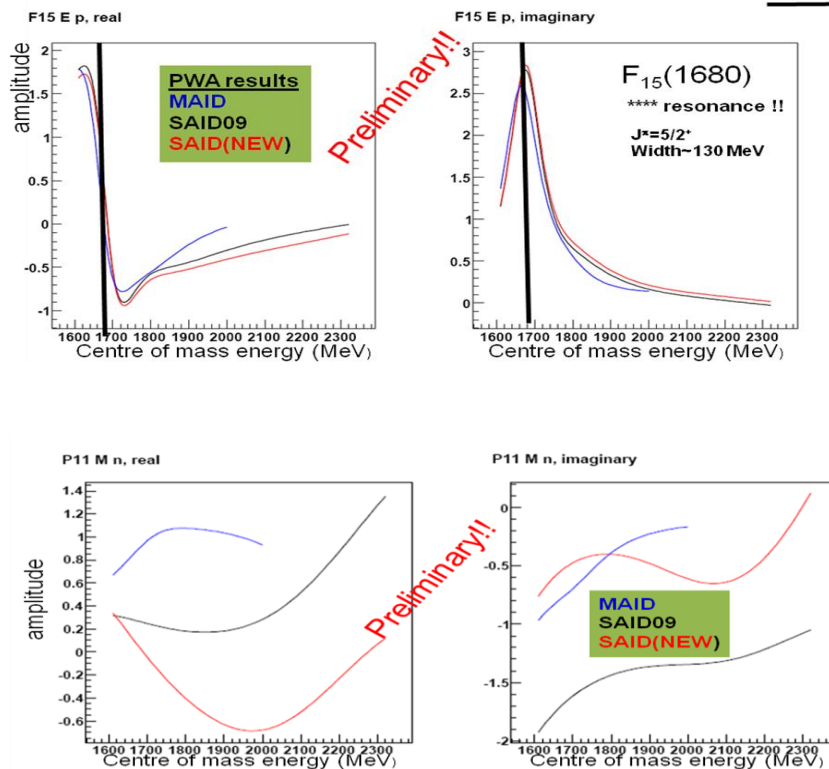


Fig 13: Upper: Partial wave analyses amplitudes extracted for the F_{15} partial wave. Lower: amplitudes for the P_{11} partial wave

Nucleon polarimeters in the sub-GeV regime typically employ nucleon-nucleus scattering. In such processes the spin-orbit potential in the interaction results in an azimuthal modulation in the yield of scattered nucleons, the amplitude of which is proportional to the degree of transverse polarisation of the incident nucleons. This is illustrated in the expression below which gives the angular dependence of the number of scattered nucleons.

$$n(\theta, \phi) = n_o(\theta) \{ 1 + A(\theta) [P_y \cos(\phi) - P_x \sin(\phi)] \}$$

No. nucleons scattered in the direction θ, ϕ
 Unpolarised polar angle distribution
 Analysing power of scatterer
 x and y (transverse) components of nucleon polarisation

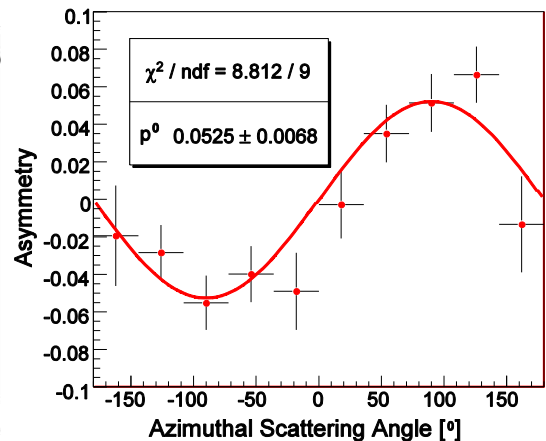
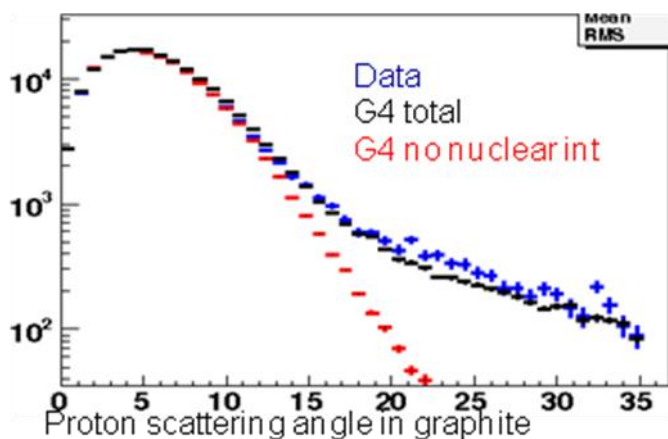
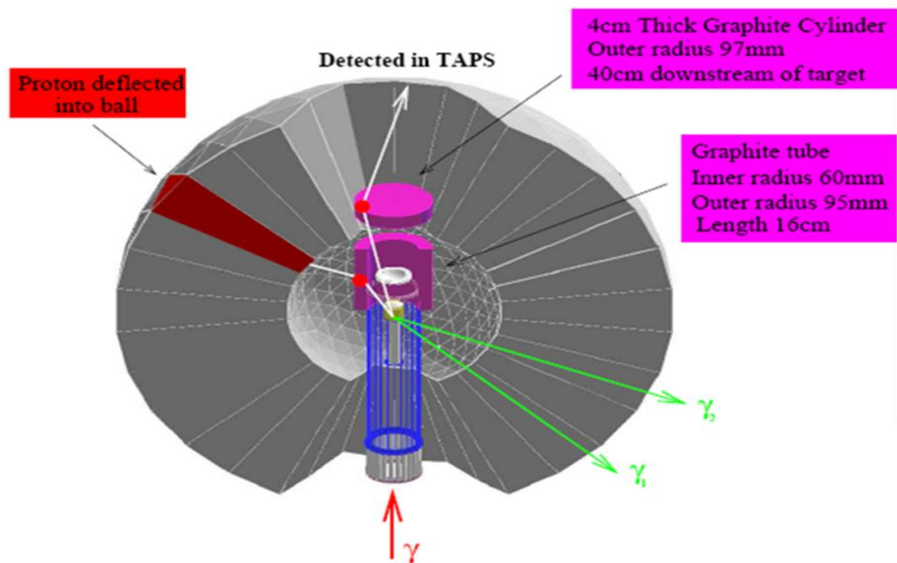


Fig 12: Left The reconstructed scatter angle of the recoiling nucleon in the polarimeter. The blue points show the data and results from a Geant4 simulation with and without nuclear scattering processes included are shown by the blue and red points respectively.

The polarimeter developed at the Crystal Ball reconstructs these scattered nucleon events kinematically using information from the incident photon, detected meson and the detected nucleon in the Crystal Ball. The operation of the device is illustrated in the lower 2 panels of Fig. 12 where the reconstructed scatter angle distribution is compared with Geant4 simulations. In the preliminary analysis, events with scatter angles greater than approx 15 degrees are selected for the sample of nuclear scattered events. The extracted azimuthal modulation of the scattered nucleons is also presented in Fig.13. Preliminary measurements of the degree of polarisation transfer from a helicity polarised photon to the recoiling nucleon in $p(\gamma, \pi^0)p$ are shown in Fig 13. At backward meson angles good agreement is observed with the current solution of the SAID partial wave analysis. However at forward angles the preliminary data indicate the partial wave solution may need to be modified to reproduce the new data.

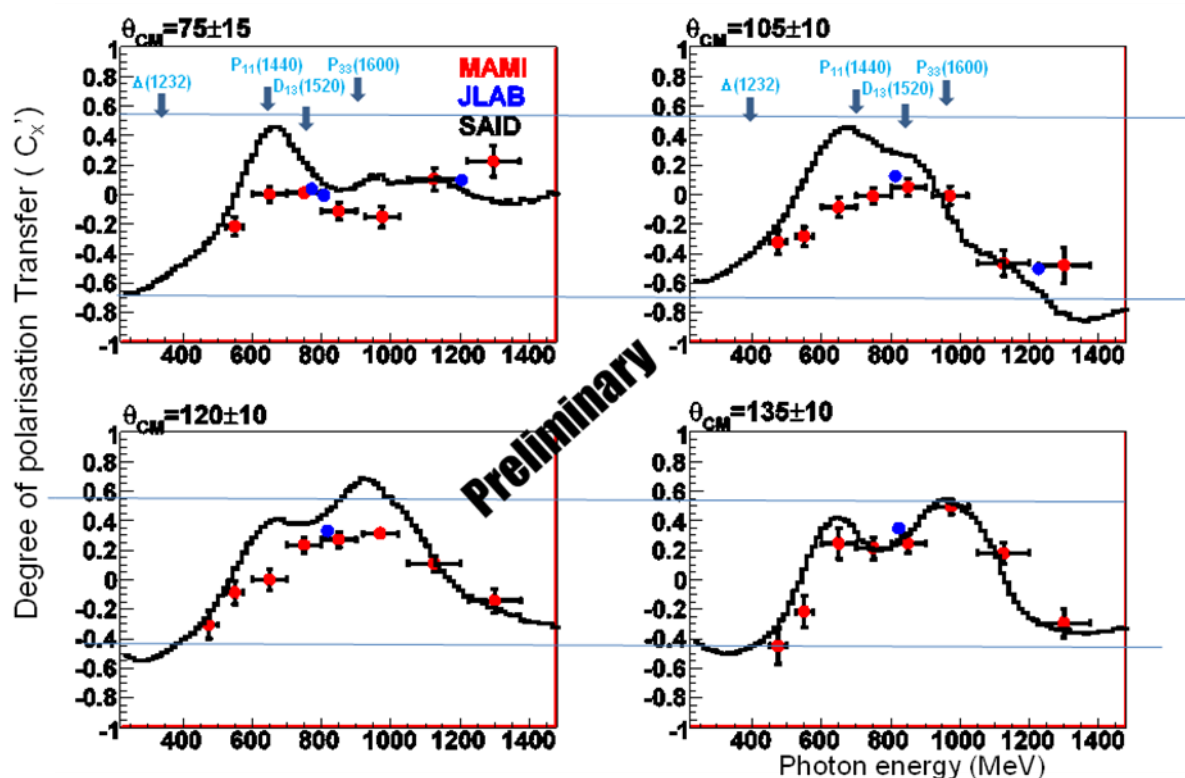


Fig 13: Preliminary results for the degree of polarisation transfer from a helicity polarised beam to the recoiling nucleon in the $p(\gamma, \pi^0)p$ reaction. The expected positions of the centre of the low lying nucleon resonances are shown in the upper two panels.

Although most of the resonances are expected to have a single pion decay branch it is important to complement studies with measurements of alternative decay branches. One of the most useful is measurements of decays to η mesons. As the η has isospin $T=0$ then only $T=1/2$ excited nucleon states can decay to an η and a nucleon. The reaction therefore serves as an isospin filter. Recent preliminary results showing the first measurement of a polarisation transfer observable in eta meson photoproduction are presented in Fig. 14. These clearly favour one of the current partial wave analysis solutions.

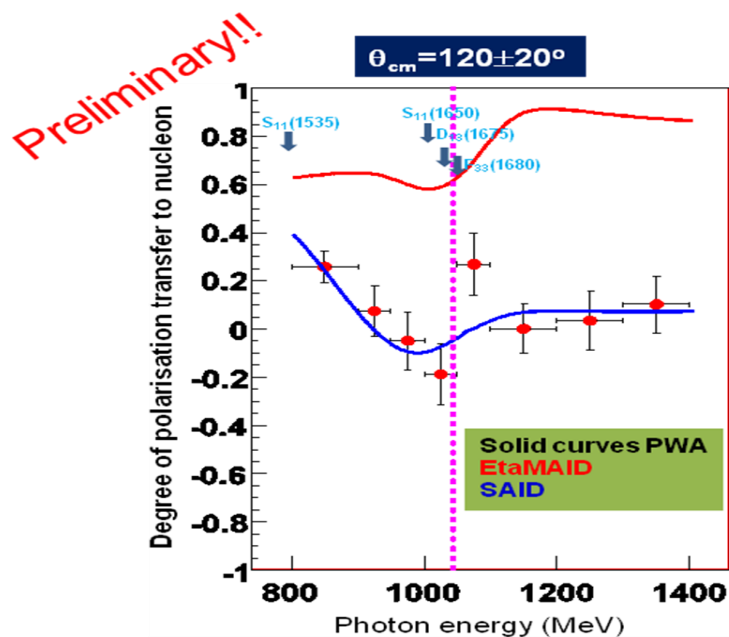


Fig 14: Preliminary results showing the polarisation transfer to the recoiling nucleon in $\gamma(p,\eta)p$ for a circularly polarised photon beam versus photon energy. The positions of low lying $T=1/2$ resonances are indicated on the figure

The programme towards the complete measurement and measurement of a range of resonance decay channels will continue in coming years. The resulting data set will provide very strong constraints on partial wave analyses and is expected to significantly improve our understanding of the fundamental excitation spectrum of the nucleon.

In summary, the photon probe programmes at the new generation of facilities offer exciting opportunities to tackle a range of fundamental open questions regarding the physics of strongly interacting matter.

[1] <http://www.kph.uni-mainz.de>

[2] <http://www.jlab.org>

[3] A. Trzcinska et. al, Phys. Rev. Lett. **87**, 08250 (2007)

[4] J. Piekarawicz., Nuc.Phys.A 778 10-21 (2006).

[5] C.J. Horowitz et al., Phys.Rev.C 63 025501.

[6] R.J. Furnstahl et. al., Nuc.Phys.A 706 85-110(2002).

[7] P. E. Haustein et. al., At. Data Nucl. Data Tables 39, 185 (1988)

[8] C Horowitz and J Piekarewicz 2001 *Phys. Rev. Lett.* **86** 5647

[9] D. Dreschel, L. Tiator, S.S. Kamalov, Shin Nan Yang, Nuc.Phys. A 660 423-438 (1999).

[10] E Klempt and J Ricard, Reviews of Modern Physics . [arXiv:0901.2055](https://arxiv.org/abs/0901.2055)

[11] N. Isgur and G. Karl, Phys. Rev. D **19**, 2653 (1979); S. Capstick and W. Roberts, Prog.

Part. Nucl. Phys. **45**, S241 (2000). F. Wilczek, arXiv:hep-ph/0409168 (2004); E. Santopinto, Phys. Rev. C **72**, 022201 (2005).

[12] F. X. Lee *et al.*, Nucl. Phys. B Proc. Suppl. **106-107**, 248 (2002); S. Sasaki, Nucl. Phys. B Proc. Suppl. **83-84**, 206 (2000); D. Brommel *et al.*, Eur. Phys. J. ST **162**, 63 (2008).

[13] S. Brodsky and G. de Teramond, Phys. Rev. Lett. **96**, 201601 (2006).

[14] L. Chang *et al.*, arXiv:0906.4304 [nucl-th] (2009).

[15] D. Sokhan, Ph.D thesis University of Edinburgh (2009)